

Morphological Control for High Performance, Solution-Processed Planar Heterojunction Perovskite Solar Cells

Giles E. Eperon, Victor M. Burlakov, Pablo Docampo, Alain Goriely, and Henry J. Snaith*

Organometal trihalide perovskite based solar cells have exhibited the highest efficiencies to-date when incorporated into mesostructured composites. However, thin solid films of a perovskite absorber should be capable of operating at the highest efficiency in a simple planar heterojunction configuration. Here, it is shown that film morphology is a critical issue in planar heterojunction $\text{CH}_3\text{NH}_3\text{PbI}_{3-x}\text{Cl}_x$ solar cells. The morphology is carefully controlled by varying processing conditions, and it is demonstrated that the highest photocurrents are attainable only with the highest perovskite surface coverages. With optimized solution based film formation, power conversion efficiencies of up to 11.4% are achieved, the first report of efficiencies above 10% in fully thin-film solution processed perovskite solar cells with no mesoporous layer.

1. Introduction

Thin-film solar cells are an important technology, promising cost-competitive solar power via reduced material and fabrication costs as compared to established crystalline silicon photovoltaics. Such systems make use of the high absorption coefficients of direct bandgap semiconductors to allow films of a few micrometers or less to absorb most incident sunlight across their bandwidth, as opposed to the hundreds of micrometers typically found in wafer based Si solar cells.^[1] High efficiencies, approaching those of crystalline silicon, have been attained for cadmium telluride (CdTe) and other compound absorbers;^[2] however, fabrication of the best performing cells relies on vacuum deposition and/or high-temperature processes, pushing potential production costs higher and limiting substrate choice.^[3] The highest performing thin-film technologies, namely CdTe and copper indium gallium (di) selenide (CIGS), additionally include elements which are in limited supply and are likely to bottleneck terawatt scale solar energy production.^[4–6] Solution-processing represents the

lowest-cost production method for thin-film solar cells. Cells can be fabricated via spin-coating, blade-coating, spraying, inkjet printing, gravure printing, or slot-dye coating.^[3,7] The highest efficiency solution-processed thin-film solar cells, reaching efficiencies of over 11%, have been achieved with solution-processable copper zinc tin chalcogenides (CZTS/Se) and CIGS bulk inorganics.^[8,9] However, the production of these solar cells relies on the use of toxic hydrazine and a high-temperature sintering process. If devices can be fully fabricated without the need for high-temperature annealing steps, greater versatility of substrate choice exists and

costs of processing and infrastructure required for manufacture could be considerably reduced. Dye-sensitized solar cells,^[10] quantum dot solar cells,^[11] and organic solar cells^[12] can be fabricated in this way, but due to fundamental energy losses associated with charge separation in a low dielectric or energetically disordered medium their theoretical maximum performances fall below those of inorganic thin-film solar cells.^[13,14]

Recently, a new family of solution-processable semiconducting perovskite structured materials based on organolead trihalide compounds have been developed, resulting in very effective sensitizers in hybrid solid-state solar cells, with published efficiencies of up to 12.3%.^[15–18] More importantly, they have been shown to exhibit ambipolar transport, allowing them to replace the hole or electron transporter in hybrid cells,^[19–21] making this family of materials suitable for solution-processable thin-film solar cells.^[15–19,21–23] Particularly, the perovskite $\text{CH}_3\text{NH}_3\text{PbI}_{3-x}\text{Cl}_x$ has been demonstrated to function in a thin-film architecture, with a layer of bulk crystalline perovskite formed over a mesoporous alumina scaffold.^[15] In previous work, planar perovskite *p-i-n* heterojunctions with no mesoporous layer gave power conversion efficiencies of up to 4.9%, while the highest power conversion efficiencies of up to 12.3% were shown in a “meso-superstructured” solar cell (MSSC) configuration with the perovskite fully infiltrating a porous alumina scaffold. However, internal quantum efficiencies of almost 100% for the planar configuration pointed towards its promise as an ultimately more efficient architecture.^[15] It is also beneficial from a production point of view to simplify the cell architecture. Hence, high efficiency cells with simply a single solution processed solid absorber layer would be advantageous.

G. E. Eperon, Dr. P. Docampo, Dr. H. J. Snaith
Department of Physics
University of Oxford, Clarendon Laboratory
Parks Road, Oxford OX1 3PU, UK
E-mail: h.snaith1@physics.ox.ac.uk
Dr. V. M. Burlakov, Prof. A. Goriely
Mathematical Institute, OCCAM
University of Oxford
24-29 St Giles, Oxford OX1 3LB, UK



DOI: 10.1002/adfm.201302090

It has been proposed that the planar thin-film architecture's lower performance may arise from pin-hole formation, incomplete coverage of the perovskite resulting in low-resistance shunting paths and lost light absorption in the solar cell; as in other technologies the issue of film formation is likely to be extremely important in the planar junction.^[24–26] It is well-known that as-fabricated thin films are often thermodynamically unstable, and likely to dewet or agglomerate upon annealing, as predicted from energetic considerations.^[27] By following the previously reported fabrication protocol for perovskite solution coating on flat substrates, we observe significant dewetting leading to incomplete coverage and non-uniform film thickness. With optimized film formation, primarily controlling the atmosphere, annealing temperature, and film thickness, we are able, for the first time, to form via solution casting uniform thin perovskite films with “full coverage” with no mesoporous layer. Doing so, we more than double the previously reported maximum power conversion efficiency in this configuration, achieving values of up to 11.4% in $\text{CH}_3\text{NH}_3\text{PbI}_{3-x}\text{Cl}_x$ planar heterojunction solar cells. This matches the best performing hydrazine processed CZTSSe thin film solar cell,^[8] and represents the first report of over 10% efficiency in this new fully thin-film solution processed perovskite technology.

2. Results and Discussion

The perovskite MSSCs studied are effectively a distributed heterojunction. The $\text{CH}_3\text{NH}_3\text{PbI}_{3-x}\text{Cl}_x$ perovskite, infiltrated within an alumina scaffold, acts as the intrinsic absorber and electron transporter, and 2,2',7,7'-tetrakis-(N,N-di-p-methoxyphenylamine)9,9'-spirobifluorene (spiro-OMeTAD) as the p-type hole transporter. Previously, the highest efficiencies have been obtained in this “infiltrated” architecture.^[15,23] A typical MSSC cell would have short-circuit current (J_{sc}) of 17–20 mA cm^{-2} , open-circuit voltage (V_{oc}) of 1.0–1.1 V, and fill factor of 0.6–0.7, which combine to result in power conversion efficiencies of above 10%.^[28] In the planar heterojunction configuration, illustrated in **Figure 1a**, J_{sc} , V_{oc} , and fill factor are lower, as shown in the current–voltage curve presented in **Figure 1b**. The significant drop in these parameters may be a result of poor coverage of perovskite films. The effects of poor coverage are twofold: firstly, if there are regions of no perovskite coverage, light will pass straight through without absorption, decreasing the available photocurrent; secondly, insufficient coverage results in a high frequency of “shunt paths” allowing contact between spiro-OMeTAD and the TiO_2 compact layer. Any such contact will act as a parallel diode in the solar cell equivalent circuit, causing a drop in V_{oc} and fill factor, and accordingly power conversion efficiency.^[29,30]

To investigate whether surface coverage is indeed an issue in this type of solar cell, we took scanning electron microscope (SEM) images of the surface morphology of perovskite films with increasingly reduced thickness of mesoporous Al_2O_3 , transitioning from the MSSC infiltrated configuration to the thin-film planar heterojunction. These SEM images are shown in **Figure 2**, and the samples were prepared in air according to the published procedure. As previously shown,^[15] we see that in addition to perovskite crystallization within the

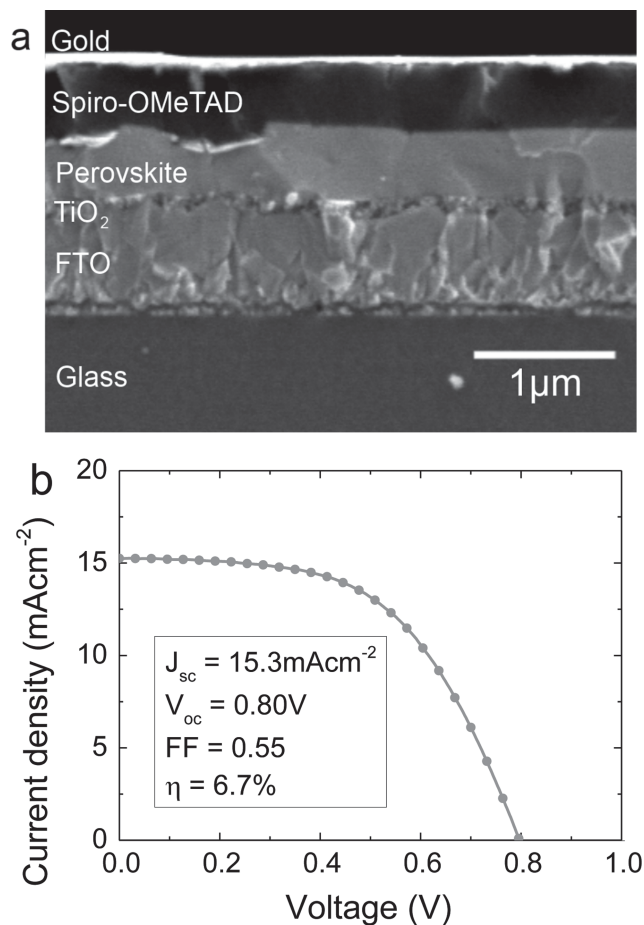


Figure 1. a) Cross-sectional SEM image showing device architecture of the planar heterojunction solar cells. b) Average current–voltage characteristics from a batch of 10 non-optimized planar heterojunction solar cells, prepared according to the published procedure,^[15] measured under simulated AM1.5 sunlight. We note that the presented JV curve is a numerical average of ten different JV curves, not simply a representative JV curve.

mesoporous layer, a perovskite “capping layer” is formed. The surface coverage of the capping layer is not complete however, and increases with decreasing alumina thickness (**Figure 2**). When the alumina is fully removed, the perovskite film forms differently, as seen in **Figure 2**. We can estimate the fractional surface coverage of perovskite, by simply setting a threshold on the image and calculating the area above and below threshold. For the films with no mesoporous layer, the surface coverage unexpectedly drops to values of $\approx 75\%$, indicating that one of the main roles of the mesoporous alumina layer is to control film formation in such a way as to produce a high coverage capping layer. When no alumina is present, the reduced perovskite coverage likely leads to the reduced J_{sc} , V_{oc} , and fill factor as suggested above. If this coverage could be increased, we would expect higher performances, possibly exceeding those from the MSSCs.

To understand why these voids are present in the perovskite layers coated on flat films, we studied a time-series of

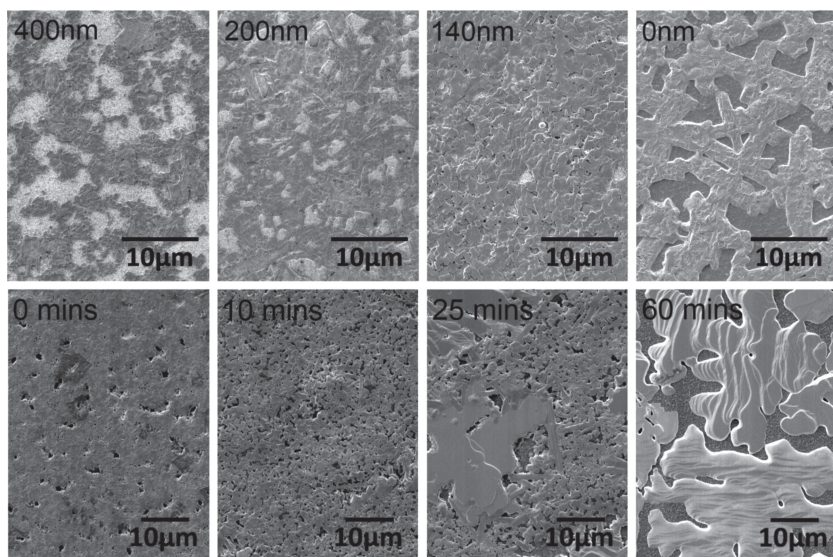


Figure 2. Top row: SEM images of the top surfaces of $\text{CH}_3\text{NH}_3\text{PbI}_{3-x}\text{Cl}_x$ films formed on alumina scaffolds of thickness shown. Bottom row: SEM images of perovskite films on compact TiO_2 -coated FTO glass with 100 °C anneal times shown on SEM images, prepared in a nitrogen atmosphere.

the perovskite anneal process, with the SEM images shown in Figure 2. Since films are extremely moisture-sensitive until fully crystallized, here we processed the films in a dry nitrogen-filled glovebox to enable characterization of the pre-crystallized films. We notice rapid degradation of non-annealed films in moist atmospheres, likely due to the hygroscopicity of the methylammonium cation.^[16] Immediately after spin-coating, film coverage is high, with a number of small pores. Upon annealing, many additional small pores form rapidly (Figure 2, 10 min), and then either increase in size or close up until the final crystalline phase is reached (Figure 2, 60 min). Upon formation of stable crystals, we observe pore evolution to cease, likely due to evaporation and mass transport no longer being energetically favorable. The morphology of samples prepared in an inert atmosphere is notably different from the air-processed samples, likely due to the lack of moisture, which otherwise attacks the surface as the film forms. We suggest that the change in the film morphology upon annealing is driven by surface energy minimization and is facilitated by mass loss.^[27] A precursor solution with an excess of methylammonium and halide compared to the lead content is used, and as such we propose then that upon spin-coating, an organic and halide-rich film is formed. As the thermal annealing process takes place, it is likely to be energetically favorable for the excess organic and halide to evaporate, once a temperature threshold is reached. This would continue until a crystal with equimolar amounts of organic, metal and halide (1:1:3 organic:metal:halide by moles) is left. Once crystallized, mass loss ceases since a low-energy state has been reached.

Depending on the conditions, we have observed the pores present in a film to either in general increase or decrease in size. Minimization of surface energy of pores is a non-trivial problem, but broadly speaking would depend upon the interaction energies of the perovskite and air, and the perovskite

and the substrate. The final crystalline morphology would depend on the dynamics of annealing, which would in turn depend on anneal temperature, solvent and mass evaporation and transport rates, and film thickness. Elsewhere, we will present a full study and mathematically model of the complex dewetting process of such solution-cast perovskite films.

Here, we form films on a fluorine-doped tin oxide (FTO) covered glass substrate coated with a TiO_2 compact layer. We can easily control film thickness and anneal temperature; film-substrate interaction energy and solvent evaporation rate are more complex to vary and quantify and so are held fixed in this study. We vary the temperature and initial thickness, and measure the resulting crystallized perovskite coverage using the image analysis software ImageJ.^[31]

SEM images of representative perovskite films are shown in Figure 3a, and the calculated coverages are plotted in Figure 3b,c. The effect of varying temperature on the wetting of the thin film is shown in Figure 3a. As

anneal temperature increases, the number of pores in the final film decreases, but their size increases and the morphology transitions from continuous layers into discrete islands of perovskite. This has the effect of reducing surface coverage, as seen in Figure 3b. Previously, annealing has been carried out at 100 °C; however this data suggests as low a temperature as possible should be used to attain maximum coverage whilst still enabling full crystallization of the perovskite absorber.

The influence of thickness variation whilst holding the temperature fixed at 95 °C is also shown in Figure 3. We see that with increasing initial film thickness, the average pore size increases, though there are fewer pores per unit area. The effect on coverage is thus not obvious; image analysis reveals that thicker initial films result in marginally greater coverages, as seen in Figure 3b. The previous standard protocol used a thickness of around 500–700 nm. This is within the expected region of high coverage; the primary factors of importance when understanding the photovoltaic behavior for these perovskite films of >200 nm thickness becomes a balance between full photon absorption and electron and hole diffusion length throughout the bulk perovskite. The detailed study of charge dynamics is beyond the scope of this report, but an experimental optimization (not detailed herein) of devices suggested thicknesses between 400 and 800 nm were suitable for attaining high efficiency devices.

Knowing the effect of these parameters, we are able to tune the desired perovskite coverage, though 100% coverage was not attainable by varying initial film thickness and temperature of anneal. To establish if increasing the perovskite coverage solves the decreases in performance seen previously, we fabricated planar heterojunction devices with a range of perovskite coverages. We varied anneal temperature, and additionally varied the solvent used to obtain the lowest coverages. Employing more slowly-evaporating solvents, dimethylsulfoxide and

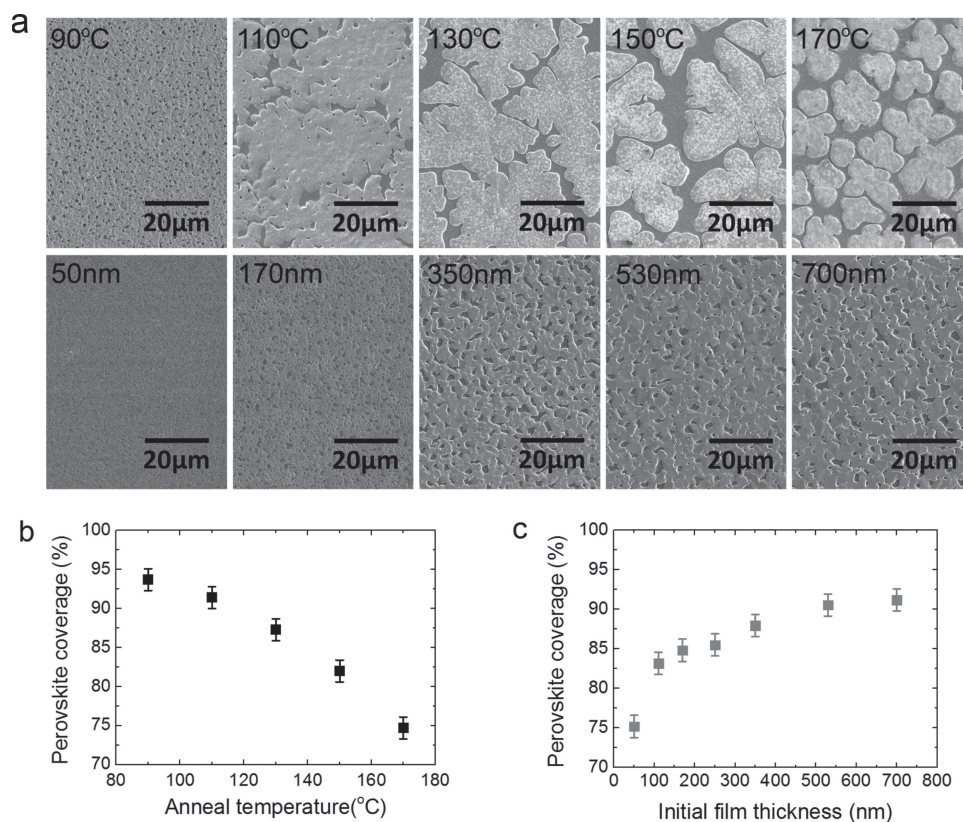


Figure 3. a) Top row: SEM images showing dependence of perovskite coverage on annealing temperature, temperature shown on images, holding initial film thickness fixed at 650 ± 50 nm. Bottom row: effect of initial perovskite film thickness, shown on images, with annealing temperature fixed at 95°C . Perovskite surface coverage as a function of b) anneal temperature and c) initial film thickness, calculated from SEM images.

n-methyl-2-pyrrolidone, instead of dimethylformamide (DMF), reduces the surface coverage.

Mean device parameters for a single batch of devices, extracted from current-voltage curves under simulated AM1.5, 100 mW cm^{-2} sunlight are shown in **Figure 4**. Short-circuit photocurrent shows a clear trend with coverage. At coverages of $\approx 56\%$, average J_{sc} is around 11 mA cm^{-2} . As the coverage increases up to $\approx 94\%$, J_{sc} increases linearly, up to average values of around 18 mA cm^{-2} . The best performing individual cells show J_{sc} above 21 mA cm^{-2} , matching the highest currents reported in the perovskite solar cells to date. The effect of coverage on power conversion efficiency, shown in **Figure 4b**, is not so clear. Despite the trend in photocurrent, fill factor and V_{oc} do not follow easily understandable trends with coverage (**Figure S2**, Supporting Information). It is likely that the changing morphology of the film additionally results in varying electronic and physical contact between hole transporter-perovskite, hole transporter-TiO₂ layer and perovskite-TiO₂ layer, which complicates the situation. However, the lowest average efficiencies are observed for the lowest coverages, and the highest average efficiencies are observed for the highest coverages. Though the intermediate behavior is not clear, our study supports the logical conclusion that high coverage is the optimum configuration for high power generation.

Motivated by this simple principle, and given that we were unable to attain 100% coverage by optimization of temperature

and thickness alone, we attempted to achieve full coverage by varying the film-substrate interaction energy. This was achieved by altering the thickness of the TiO₂ compact layer. Indeed, we observed that by using thicker TiO₂ compact layers, increased coverage was attained. Representative films are shown in **Figure 5**. This discovery enabled us to produce full-coverage perovskite films. We currently propose that the n-type compact layer interacts electronically with the perovskite film during formation; possibly a thicker layer is able to transfer more electronic charge to the perovskite assisting its formation near the surface due to differing electrostatics. However, we note this is purely speculative and further investigation of this important effect is currently in progress.

We fabricated devices from a range of TiO₂ compact layer thicknesses, measuring perovskite coverage and device parameters to determine if any additional gains in efficiency are seen compared to 90%+ coverage. TiO₂ compact layer thickness was varied by repeatedly spin-coating more layers of the TiO₂ precursor solution. A single spin-coated layer was measured to be approximately 75 nm thick. **Figure 5d** shows the dependence of perovskite coverage, J_{sc} , power conversion efficiency and V_{oc} on increased TiO₂ compact layer thickness. With thicker TiO₂ layers, an increase in perovskite coverage is seen; however, disappointingly both J_{sc} and V_{oc} drop, resulting in lower device efficiencies. A TiO₂ compact layer of increased thickness is likely to have a significant effect upon

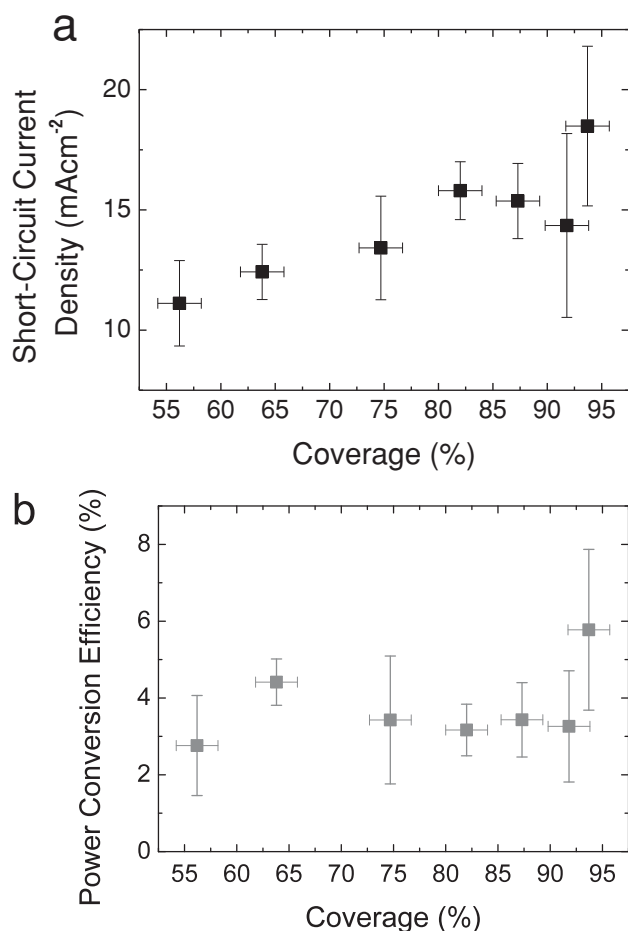


Figure 4. Dependence of the a) short-circuit current density and b) power conversion efficiency on perovskite coverage, extracted from solar cells illuminated under simulated AM1.5 sunlight of 100 mW cm⁻² irradiance. Each data point represents the mean from a set of 9 or more individual devices.

device performance since the relatively resistive, and possibly depleted TiO₂ layer is critical to electron collection. Thick TiO₂ compact layers have been shown previously to hinder charge extraction in dye-sensitized solar cells due to increased series resistance;^[32] this is likely to be the reason for the observed decrease in performance here.

Despite not achieving further improvements in efficiency with full coverage based on thicker TiO₂ compact layers, we obtained impressive efficiencies with the highest perovskite coverages on the thinnest TiO₂ layer. This was achieved by annealing at a lower temperature of 90 °C, with an initial perovskite film thickness of 450–550 nm. The improvement in average current-voltage characteristics, and hence overall performance resulting from this process is shown in **Figure 6a**. The current-voltage curve corresponding to the most efficient device measured is shown in **Figure 6b**. The efficiency of the most efficient device is 11.4%, which represents greater than a two-fold improvement over the previous report of solution processed planar heterojunction

perovskite solar cells.^[15] Improvements are due to increased J_{sc} , V_{oc} , and fill factor, and are likely to stem from two effects resulting from improved perovskite coverage. Firstly, it has enabled collection of a higher fraction of incident photons, increasing useful current generated. Secondly, the increased coverage has reduced contact area between the hole transporter and the n-type TiO₂ compact layer, which removes a shunt path previously leading to leakage currents.^[33] Reduction of these shunt paths would therefore be expected to enhance the fill factor and V_{oc} as we observe here. Full elimination of shunt paths may be expected to increase V_{oc} up to levels seen in the MSSC configuration ($\approx 1.1V$). We expect that further tuning of the interaction energy between the TiO₂ compact layer and the perovskite, whilst still employing thin TiO₂ films, will enable 100% perovskite coverage upon electronically optimal layers, resulting in further enhanced performance.

3. Conclusions

By understanding and controlling morphology of perovskite films originating from a non-stoichiometric composition of precursor salts, we have demonstrated the critical role of uniform perovskite film formation in planar heterojunction perovskite solar cells. The highest efficiencies are achievable only with the highest surface coverages. We have fabricated flat heterojunction cells at low temperatures with efficiencies of up to 11.4%, the first report of a fully thin-film solution processed perovskite solar cell with no mesoporous layer with efficiency above 10%. This indicates that a mesoporous layer is no longer necessary to achieve high efficiency perovskite cells. Simplification of the cell architecture in this way increases the versatility of such cells, and can enable easier and cheaper manufacturing on a large scale. There is immense scope for further research to lead to even higher efficiency planar heterojunction perovskite cells.

4. Experimental Section

Perovskite Precursor Preparation: Methylamine iodide (MAI) was prepared by reacting methylamine, 33 wt% in ethanol (Sigma-Aldrich), with hydroiodic acid (HI) 57 wt% in water (Sigma-Aldrich), at room temperature. HI was added dropwise while stirring. Upon drying at 100 °C, a white powder was formed, which was dried overnight in a vacuum oven before use. To form the non-stoichiometric CH₃NH₃PbI_{3-x}Cl_x precursor solution, methylammonium iodide and lead (II) chloride (Sigma-Aldrich) are dissolved in anhydrous *N,N*-Dimethylformamide (DMF), dimethylsulfoxide (DMSO), or *n*-methyl-2-pyrrolidone (NMP) at a 3:1 molar ratio of MAI to PbCl₂, with final concentrations 0.88 M lead chloride and 2.64 M methylammonium iodide. This solution is stored under a dry nitrogen atmosphere. As shown in **Figure S1** (Supporting Information), the X-ray diffraction data from this perovskite shows a highly crystalline material with peaks as in the previously reported data.^[15,20]

Substrate Preparation: Devices were fabricated on fluorine-doped tin oxide (FTO) coated glass (Pilkington, 7Ω □⁻¹). Initially FTO was removed from regions under the anode contact, to prevent shunting upon contact with measurement pins, by etching the FTO with 2 M HCl and zinc powder. Substrates were then cleaned sequentially in 2% hallmanex detergent, acetone, propan-2-ol and oxygen plasma. A

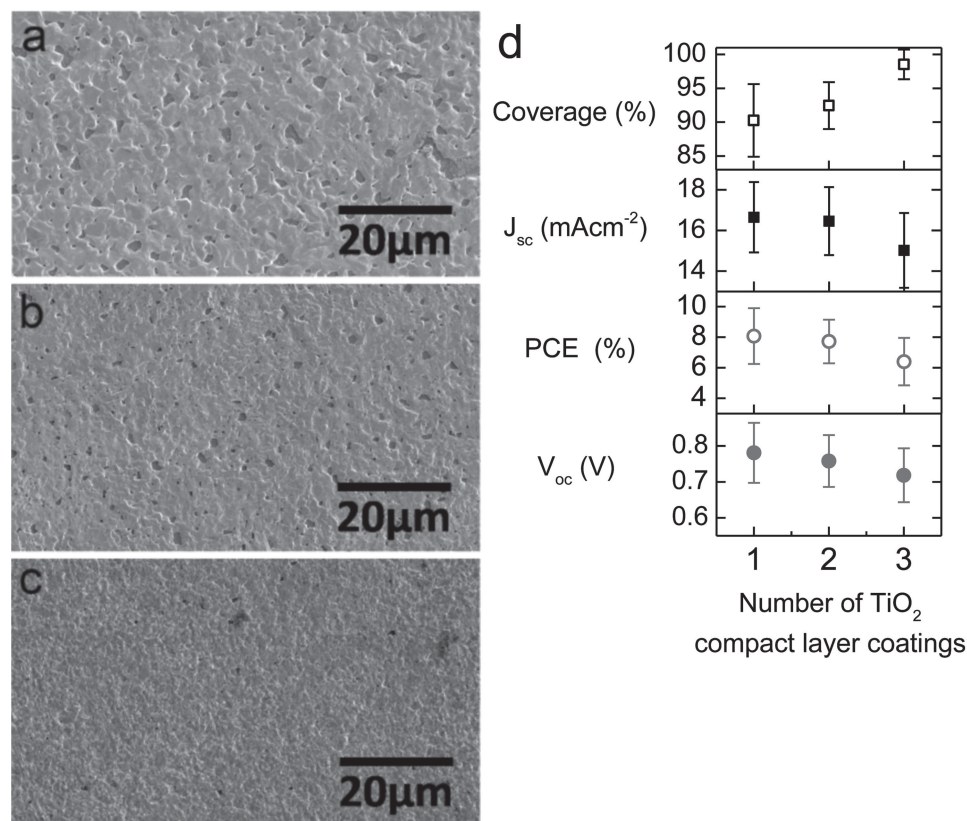


Figure 5. a–c) SEM images of perovskite films formed on a) ≈ 75 nm, b) ≈ 150 nm, and c) ≈ 225 nm thick TiO₂ compact layers coating FTO substrates. d) Dependence of perovskite coverage and device performance parameters on the thickness of the TiO₂ compact layers, in a single batch of devices. Each data point represents the mean from 32 or more individual devices, with the exception of coverage, which is based on three measurements per data point.

hole-blocking layer of compact TiO₂ was deposited by spin-coating a mildly acidic solution of titanium isopropoxide in ethanol, and annealed at 500 °C for 30 min. Spin-coating was carried out at 2000 rpm for 60 s.

Perovskite Solar Cell Fabrication: To form the perovskite layer, the non-stoichiometric precursor was spin-coated on the substrate in a nitrogen-filled glovebox, at 2000 rpm for 45 s. To vary the initial layer thickness, the precursor was diluted in DMF, or the spin speed varied. After spin-coating, the films were left to dry at room temperature in the glovebox for 30 minutes, to allow slow solvent evaporation. They were then annealed on a hotplate in the glovebox at 90 °C, 110 °C, 130 °C, 150 °C, or 170 °C, for 120, 50, 20, 10, or 7.5 min respectively.

A hole-transporting layer was then deposited in air via spin-coating a 0.79 M solution of 2,2',7,7'-tetrakis-(N,N-di-p-methoxyphenylamine)9,9'-spirobifluorene (spiro-OMeTAD) in chlorobenzene, with additives of lithium bis(trifluoromethanesulfonyl) imide and 4-tert-butylpyridine. Spin-coating was carried out at 2000 rpm for 60 s. Devices were then left overnight in air for the spiro-OMeTAD to dope via oxidation.^[34] Finally, 60 nm gold electrodes were thermally evaporated under vacuum of $\approx 10^{-6}$ Torr, at a rate of ≈ 0.1 nm s⁻¹, to complete the devices.

Materials Characterization: A field emission scanning electron microscope (Hitachi S-4300) was used to acquire SEM images. To acquire images of moisture-sensitive unannealed perovskite films, samples were kept in nitrogen atmosphere until imaging. To determine coverage of perovskite films from SEM images, ImageJ^[30] was used to define a greyscale threshold such that the perovskite was distinct from the substrate, and percentage coverage was then calculated by the program. Sample thicknesses were measured using a Veeco Dektak 150 surface profilometer. X-ray diffraction (XRD) spectra were obtained from

full devices with no evaporated electrodes, using a Panalytical X'Pert Pro x-ray diffractometer.

Solar Cell Characterization: The current density–voltage (J–V) curves were measured (2400 Series SourceMeter, Keithley Instruments) under simulated AM 1.5 sunlight at 100 mW cm⁻² irradiance generated by an Abet Class AAB sun 2000 simulator, with the intensity calibrated with an NREL calibrated KG5 filtered Si reference cell. The mismatch factor was calculated to be less than 1%. The solar cells were masked with a metal aperture to define the active area, typically 0.09 cm⁻² (measured individually for each mask) and measured in a light-tight sample holder to minimize any edge effects and ensure that the reference cell and test cell are located during measurement in the same spot under the solar simulator.

Supporting Information

Supporting Information is available from the Wiley Online Library or from the author.

Acknowledgements

This work was supported by EPSRC and Oxford Photovoltaics Ltd. through a Nanotechnology KTN CASE award, the European Research Council (ERC) HYPER PROJECT no. 279881. This publication is based in part upon work supported by Award No. KUK-C1-013-04, made by King Abdullah University of Science and Technology (KAUST). A.G. is a Wolfson/Royal Society Merit Award Holder and acknowledges support

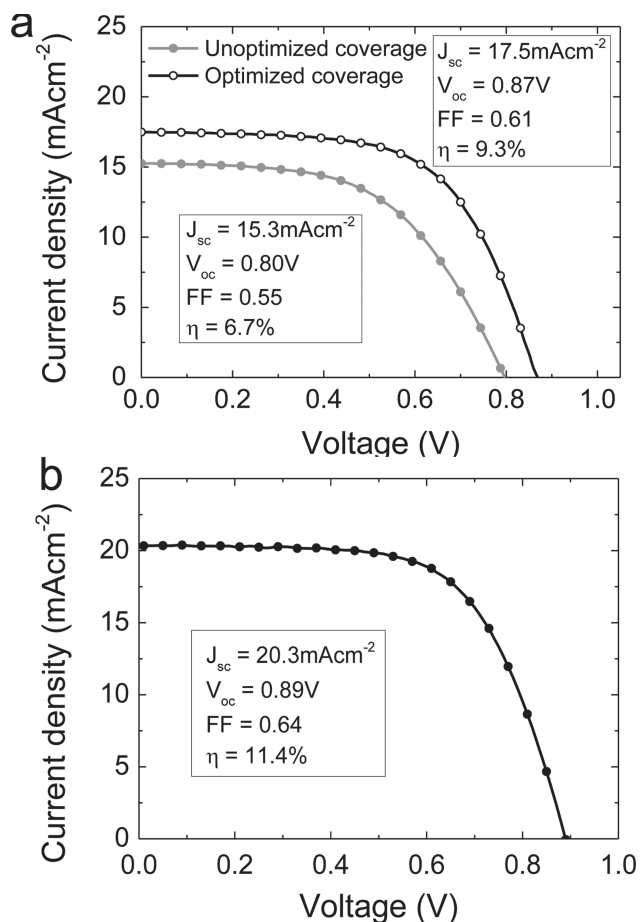


Figure 6. Current–voltage characteristics measured under simulated AM1.5, 100 mW cm⁻² sunlight of a) the average of a batch of 11 solar cells produced using the optimized high coverage planar heterojunction configuration, compared to the previously shown unoptimized batch and b) the best performing solar cell based on the planar heterojunction configuration.

from a Reintegration Grant under EC Framework VII. V.B. is an Oxford Martin School Fellow and this work was in part supported by the Oxford Martin School. The authors would like to thank Edward Crossland and James Ball for valuable discussions.

Received: June 19, 2013

Revised: July 15, 2013

Published online:

- [1] D. B. Mitzi, O. Gunawan, T. K. Todorov, K. Wang, S. Guha, *Sol. Energy Mater. Sol. Cells* **2011**, *95*, 1421.
 [2] M. A. Green, K. Emery, Y. Hishikawa, W. Warta, E. D. Dunlop, *Prog. Photovoltaics: Res. Appl.* **2013**, *21*, 1.

- [3] M. Grätzel, R. A. J. Janssen, D. B. Mitzi, E. H. Sargent, *Nature* **2012**, *488*, 304.
 [4] A. Bosio, D. Menossi, S. Mazzamuto, N. Romeo, *Thin Solid Films* **2011**, *519*, 7522.
 [5] R. N. Bhattacharya, M. A. Contreras, B. Egaas, R. N. Noufi, A. Kaneve, J. R. Sites, *Appl. Phys. Lett.* **2006**, *89*, 253503.
 [6] V. Fthenakis, *Renewable Sustainable Energy Rev.* **2009**, *13*, 2746.
 [7] F. C. Krebs, *Sol. Energy Mater. Sol. Cells* **2009**, *93*, 394.
 [8] D. A. R. Barkhouse, O. Gunawan, T. Gokmen, T. K. Todorov, D. B. Mitzi, *Prog. Photovoltaics: Res. Appl.* **2012**, *20*, 6.
 [9] T. K. Todorov, O. Gunawan, T. Gokmen, D. B. Mitzi, *Prog. Photovoltaics: Res. Appl.* **2013**, *21*, 82.
 [10] M. K. Nazeeruddin, E. Baranoff, M. Grätzel, *Sol. Energy* **2011**, *85*, 1172.
 [11] E. H. Sargent, *Nat. Photonics* **2012**, *6*, 133.
 [12] J. Nelson, *Mater. Today* **2011**, *14*, 462.
 [13] H. J. Snaith, *Adv. Funct. Mater.* **2010**, *20*, 13.
 [14] T. Kirchartz, K. Taretto, U. Rau, *J. Phys. Chem. C* **2009**, *113*, 17958.
 [15] J. M. Ball, M. M. Lee, A. Hey, H. J. Snaith, *Energy Environ. Sci.* **2013**, *6*, 1739.
 [16] J. H. Noh, S. H. Im, J. H. Heo, T. N. Mandal, S. I. Seok, *Nano Lett.* **2013**, *13*, 1764.
 [17] H.-S. Kim, C.-R. Lee, J.-H. Im, K.-B. Lee, T. Moehl, A. Marchioro, S.-J. Moon, R. Humphry-Baker, J.-H. Yum, J. E. Moser, M. Grätzel, N.-G. Park, *Sci. Rep.* **2012**, *2*, 591.
 [18] A. Kojima, K. Teshima, Y. Shirai, T. Miyasaka, *J. Am. Chem. Soc.* **2009**, *131*, 6050.
 [19] I. Chung, B. Lee, J. He, R. P. H. Chang, M. G. Kanatzidis, *Nature* **2012**, *485*, 486.
 [20] M. M. Lee, J. Teuscher, T. Miyasaka, T. N. Murakami, H. J. Snaith, *Science* **2012**, *338*, 643.
 [21] L. Etgar, P. Gao, Z. Xue, Q. Peng, A. K. Chandiran, B. Liu, M. K. Nazeeruddin, M. Grätzel, *J. Am. Chem. Soc.* **2012**, *134*, 17396.
 [22] J.-H. Im, C.-R. Lee, J.-W. Lee, S.-W. Park, N.-G. Park, *Nanoscale* **2011**, *3*, 4088.
 [23] M. M. Lee, J. Teuscher, T. Miyasaka, T. N. Murakami, H. J. Snaith, *Science* **2012**, *338*, 643.
 [24] X. Yang, J. Loos, *Macromolecules* **2007**, *40*, 1353.
 [25] Z.-S. Wang, H. Kawauchi, T. Kashima, H. Arakawa, *Coord. Chem. Rev.* **2004**, *248*, 1381.
 [26] W. Jaegermann, A. Klein, T. Mayer, *Adv. Mater.* **2009**, *21*, 4196.
 [27] C. V. Thompson, *Ann. Rev. Mater. Res.* **2012**, *42*, 399.
 [28] H. J. Snaith, *Energy Environ. Sci.* **2012**, *5*, 6513.
 [29] P. Docampo, H. J. Snaith, *Nanotechnology* **2011**, *22*, 225403.
 [30] L. Han, N. Koide, Y. Chiba, T. Mitate, *Appl. Phys. Lett.* **2004**, *84*, 2433.
 [31] W. Rasband, ImageJ **2005**, <http://rsb.info.nih.gov/ij/>, accessed: August 2013.
 [32] B. Peng, G. Jungmann, C. Jäger, D. Haarer, H.-W. Schmidt, M. Thelakkat, *Coord. Chem. Rev.* **2004**, *248*, 1479.
 [33] H. J. Snaith, N. C. Greenham, R. H. Friend, *Adv. Mater.* **2004**, *16*, 1640.
 [34] A. Abate, T. Leijtens, S. Pathak, J. Teuscher, R. Avolio, M. E. Errico, J. Kirkpatrick, J. M. Ball, P. Docampo, I. McPherson, H. J. Snaith, *Phys. Chem. Chem. Phys.* **2013**, *15*, 2572.